ROYAL SOCIETY
OF CHEMISTRY

## PAPER

# Second near-infrared photoactivatable biocompatible polymer nanoparticles for effective *in vitro* and *in vivo* cancer theranostics†

Fei Wang,‡[a] Xiaoju Men,‡[b] Haobin Chen, [ID][c] Feixue Mi,[c] Mengze Xu,[b] Xiaoxiao Men,[c] Zhen Yuan*[b] and Pik Kwan Lo [ID] *[a,d]

Photoacoustic imaging (PAI)-guided photothermal therapy (PTT) has drawn considerable attention due to the deeper tissue penetration and higher maximum permissible exposure. However, current photothera-nostic agents are greatly restricted by weak absorption in the second near-infrared (NIR-II, 1000–1700 nm) window, long-term toxicity, and poor photostability. In this report, novel organic NIR-II conjugated polymer nanoparticles (CPNs) based on narrow bandgap donor−acceptor BDT-TBZ polymers were developed for effective cancer PAI and PTT. Characterization data confirmed the high photothermal conversion efficiency, good photostability, excellent PAI performance, and superior biocompatibility of as-obtained CPNs. In addition, *in vitro* and *in vivo* tests demonstrated the efficient PTT effect of CPNs in ablating cancer cells and inhibiting tumor growth under 1064 nm laser irradiation. More importantly, the CPNs exhibited rapid clearance capability through the biliary pathway and negligible systematic toxicity. Thus, this work provides a novel organic theranostic nanoplatform for NIR-II PAI-guided PTT, which advances the future clinical translation of biocompatible and metabolizable conjugated nanomaterials in cancer diagnosis and therapy.

## 1. Introduction

Cancer has currently been a great challenge to worldwide public health as a life-threatening disease with a high mortality rate.[1] Due to serious side effects and poor therapeutic outcome of the traditional cancer therapies, the development of novel and efficient therapies with good patient compliance is of urgency and importance. Among diverse cancer therapeutic modalities, photothermal therapy (PTT), in which light is converted into thermal energy by PTT agents to ablate cancer cells or deep tissue solid tumors, has attracted considerable research interest due to its high specificity, minimal invasiveness, easy operability, and favorable therapeutic outcome.[2,3] Another approach to mitigate the suffering of

patients is to facilitate therapeutic accuracy by introducing molecular imaging technologies in the process of cancer treatment and prognosis. Consequently, various medical imaging methodologies have been widely exploited and utilized in a variety of preclinical or clinical studies.[4–6] Particularly, photoacoustic (PA) imaging (PAI), which integrates optical excitation and ultrasonic detection based on the photoacoustic effect, holds great promise for physiological and pathological visualization because of the superior advantages of deeper tissue penetration depth, better absorption contrasts, and higher spatiotemporal resolution.[7] Interestingly, both PTT and PAI are developed based on the heat generation of the light-absorbing agents, driving the integration of PTT and PAI into one single platform for the beneficial imaging-guided cancer therapy.[8–10]

Near-infrared (NIR) light has gradually been introduced into the advancement of PAI-guided PTT owing to the unparalleled advantages of reduced scattering and absorption and remote manipulation in the biological tissues, as compared to visible light.[11] Diverse NIR light-responsive PTT/PAI agents, such as carbon nanoparticles,[12,13] quantum dots,[14–16] metal-based nanomaterials,[17–20] and small molecules,[21–25] have been investigated for proof-of-concept PAI-guided PTT applications. However, some uncertainties in terms of *in vivo* long-term toxicity and metabolism of the inorganic nanoparticles, poor

*[a] Department of Chemistry, City University of Hong Kong, Tat Chee Avenue, Kowloon Tong, Hong Kong, SAR, China. E-mail: peggylo@cityu.edu.hk*
*[b] Faculty of Health Sciences, Center for Cognitive and Brain Sciences, University of Macau, Macau, SAR 999078, China. E-mail: zhenyuan@um.edu.mo*
*[c] Department of Biomedical Engineering, Southern University of Science and Technology, Shenzhen, Guangdong 518055, China*
*[d] Key Laboratory of Biochip Technology, Biotech and Health Care, Shenzhen Research Institute of City University of Hong Kong, Shenzhen, Guangdong 518057, China*
†Electronic supplementary information (ESI) available. See DOI: 10.1039/d1nr03156b
‡These authors contributed equally to this work.

photostability and efficacy of the small molecules highly restricted to their practical applications in clinical trials. In addition, existing PTT/PAI agents are mainly focus on the first NIR (NIR-I, 700–900 nm) biological window, urging the efforts to extend the wavelength to the second NIR (NIR-II, 1000–1700 nm) window for deeper tissue penetration and higher maximum permissible exposure (MPE).[26,27] Therefore, developing novel nanoplatforms functioning as both PTT and PAI agents with superior biocompatibility and excellent photostability, especially responsive to the NIR-II light, remains a great challenge.

Conjugated polymer nanoparticles (CPNs), dominantly composed of π-conjugated motifs, represent promising type of organic nanoparticles because of their attractive characteristics, including large absorption coefficients, high fluorescence brightness, narrow size distribution, excellent colloidal stability, and superior biocompatibility.[28–30] In the past two decades, various CPNs have been designed and demonstrated their utility in wide-ranging biological and biomedical applications, including cell labeling and tracking,[31,32] bioimaging,[33–35] sensing and detection,[36,37] drug delivery,[38–40] photoacoustic imaging,[7,41,42] and therapy.[43,44] Because of the versatile donor–acceptor (D–A) structure, the chemical and optical properties of CPNs can be easily tuned by altering the donor or acceptor moiety on the polymer backbone. More importantly, CPNs with high photothermal conversion efficiency (PCE) in the NIR region could be designed and prepared as effective PTT and PAI nanoagents via the bandgap engineering approach. For example, Chen and coworkers demonstrated that CPNs exhibiting tunable NIR absorption peaks can function as both PTT and PAI nanoplatforms for cancer theranostics.[45] Furthermore, Pu's group reported the attempt of utilizing conjugated polymer nanoparticles with absorption peaks in both NIR windows for PTT applications, indicating the superiority and importance of tuning the absorptive wavelength from the NIR-I window into the NIR-II window for deep-tissue cancer PTT.[27] Up to now, CPNs displaying strong absorption in the NIR-II window received extensive attention for cancer diagnosis and therapy but relevant investigations are still limited and not adequately understood. Accordingly, the development of CPNs with strong absorption in the NIR-II window and the follow-up exploration of their performance in PAI-guided cancer PTT is highly desirable.

In this work, we designed and synthesized NIR-II highly absorptive conjugated polymers (BDT-TBZ) with narrow bandgap D–A form. The polymers were assembled into CPN via a nanoprecipitation approach (Fig. 1), which possessed strong absorption in the NIR-II window, remarkable colloidal stability, excellent biocompatibility, and high photothermal conversion efficiency under NIR-II 1064 nm laser irradiation. The PAI tests further indicated the strong photoacoustic signal generation ability of BDT-TBZ CPNs, showing higher PA signal intensity enhancement than our previously reported PA nanoagents for intratumoral injection. The in vitro cellular and in vivo animal PPT experiments demonstrated the remarkable
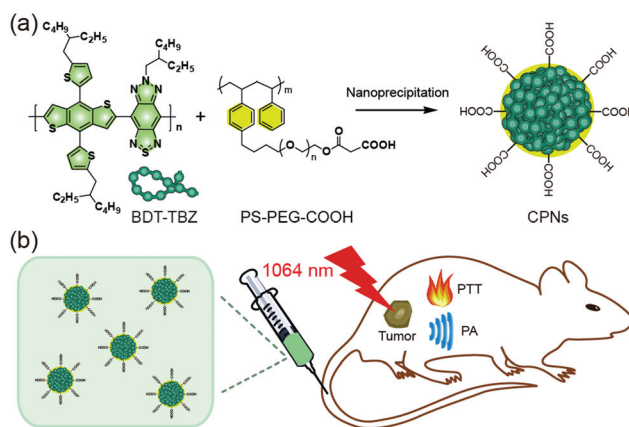


**Fig. 1** (a) Chemical structure of the conjugated polymer BDT-TBZ and functional polymer PS-PEG-COOH and schematic illustration of CPNs preparation via a nanoprecipitation approach. (b) Schematic illustration of BDT-TBZ CPNs for second near-infrared photoacoustic imaging-guided photothermal cancer therapy.

photothermal therapeutic effect of BDT-TBZ CPNs under 1064 nm laser irradiation. In addition, the in vivo biodistribution and potential toxicology assays highlighted the body clearance capability and negligible toxicity of as-obtained CPNs. Taken together, our work demonstrates the capability of BDT-TBZ CPNs as biocompatible nanoplatforms for NIR-II PAI-guided PTT, broadening the diversity of the theranostic nanoagents for cancer diagnosis and therapy.

## 2.  Experimental

### 2.1  Materials

3-(4,5-Dimethylthiazol-2-yl)-2,5-diphenyltetrazolium bromide (MTT), tetrahydrofuran (THF), and dimethyl sulfoxide (DMSO) were purchased from Sigma-Aldrich. Fetal bovine serum (FBS), Dulbecco's Modified Eagle Medium (DMEM), phosphate buffered saline (PBS, pH 7.4), penicillin streptomycin solution, trypsin, calcein acetoxymethyl ester (calcein/AM) and propidium iodide (PI) were purchased from Invitrogen. The functional polymer, polystyrene-polyethylene glycol-carboxyl (PS-PEG-COOH) was purchased from Polymer Source Inc., Canada. Ultrapure $H_2O$ was used in this study. All chemicals were used as received without purification unless indicated.

### 2.2  Synthesis of conjugated polymer BDT-TBZ

The new conjugated polymer BDT-TBZ was synthesized by conjugating the donor monomer benzodithiophene (BDT) and the acceptor monomer thiadiazolobenzotriazole (TBZ) via a reported Stille coupling polymerization.[45] The detailed procedure is provided in the ESI.†

### 2.3  Preparation and characterization of BDT-TBZ CPNs

BDT-TBZ CPNs were prepared via a modified nanoprecipitation approach as previously reported.[46] Typically, 3 mL THF homogeneous solution containing BDT-TBZ polymers (100 µg

mL$^{-1}$) and PS-PEG-COOH (25 μg mL$^{-1}$) was rapidly injected into 10 mL ultrapure water under vigorous sonication. After that, THF was removed from the dispersion by heated on a hotplate with N$_2$ stripping. The obtained BDT-TBZ CPNs were filtered through a 0.22 μm membrane filter and then purified with an Econo-Pac 10DG filtration column. The silicon 2,3-naphthalocyanine bis(trihexylsilyloxide) (NIR775)-doped CPNs were also prepared for fluorescence imaging. The as-prepared BDT-TBZ CPNs were stored at 4 °C for further use. The morphology of BDT-TBZ CPNs was studied using a transmission electron microscopy (TEM) (Philips Technai 12). Dynamic light scattering (DLS) measurements were conducted on a Malvern Mastersizer (Malvern Zetasizer Nano ZS) to study the size distribution and surface zeta potential of BDT-TBZ CPNs. The absorption spectra of BDT-TBZ CPNs was acquired on an ultraviolet-visible-near infrared spectrophotometer (Evolution 300). A 1064 nm diode-pumped solid-state laser system was employed to determine the photothermal properties of BDT-TBZ CPNs. The thermal images were collected using an infrared camera (SC300, Fluke TiR), and then analyzed with the Guide Infrared Analysis software.

### 2.4 Cell culture

Human breast cancer MCF-7 cell and mouse mammary carcinoma 4T1 cell lines were obtained from the American Type Culture Collection, USA. The cells were cultured in DMEM medium supplemented with 10% FBS, penicillin (100 U mL$^{-1}$), and streptomycin (100 μg mL$^{-1}$). The cells were incubated at 5% CO$_2$ in a humidified atmosphere at 37 °C, and routinely passaged *via* a trypsin-dependent approach.

### 2.5 *In vitro* cytotoxicity assay

The *in vitro* cytotoxicity of BDT-TBZ CPNs was determined by MTT assay. Typically, MCF-7 or 4T1 cells were seeded in a 96-well plate with 10 000 cells per well and incubated overnight. The culture medium was refreshed with medium containing BDT-TBZ CPNs of various concentrations (0, 10, 25, 50, and 100 μg mL$^{-1}$), and the cells were further incubated for 24 h or 48 h, respectively. Thereafter, 20 μL MTT of 5 mg mL$^{-1}$ in PBS was added into each well and the cells were incubated for another 4 h. The medium was then discarded, and 200 μL DMSO was added into each well. The plate was incubated in darkness for 30 min at 37 °C and the absorbance at 570 nm was subsequently recorded with a Cytation 3 microplate reader (Bio-Tek). The obtained data was calculated and shown as mean ± SD deviation ($n$ = 6).

### 2.6 *In vitro* PTT assessment

The *in vitro* PTT therapy of BDT-TBZ CPNs against cancer cells was studied *via* MTT assays. For the MTT assay, MCF-7 or 4T1 cells were seeded in a 96-well plate and incubated to reach 80% confluent. Then, fresh medium containing BDT-TBZ CPNs of various concentrations (0, 25, 50, and 100 μg mL$^{-1}$) was added and the cells were incubated for 12 h. Afterwards, the cells were treated with irradiation of a 1064 nm laser with a power density of 1 W cm$^{-2}$ for 6 min, and cells were then

incubated for another 12 h. Cell viability was then determined *via* described MTT approach. Cells incubated in darkness at 37 °C for 6 min were set as control groups.

### 2.7 Living/dead cell staining assay

The MCF-7 cells were plated into 35 mm glass-bottomed confocal dishes and incubated to reach 80% confluent. Then, the culture medium was replaced with fresh medium containing BDT-TBZ CPNs and the cells were incubated for another 12 h. The cells were subsequently illuminated with a 1064 nm laser (1 W cm$^{-2}$) for 6 min, and cells were incubated for an additional 4 h. Cells received no treatment or CPNs incubation or laser irradiation were set as control groups. After that, cells were washed twice with PBS solution and then stained with calcein-AM and PI for 30 min. Living and dead cells could be stained by calcein-AM (green fluorescence) or PI (red fluorescence), respectively. Confocal cell imaging was conducted immediately after cell staining with a Leica TCS SP5 laser confocal scanning microscope.

### 2.8 Tumor mouse model

All animal procedures were performed in accordance with the Guidelines for Care and Use of Laboratory Animals of City University of Hong Kong and approved by the Animal Ethics Committee of City University of Hong Kong. Female Balb/c nude mice (6–8 weeks) were obtained from and then housed in the Laboratory Animal Research Unit (LARU), City University of Hong Kong in a pathogen-free environment. The 4T1 tumor mouse model was established *via* injection of 5 × 10$^6$ 4T1 cells in 100 μl PBS solution subcutaneously into left flank of Balb/c nude mice.

### 2.9 Photoacoustic imaging

The *in vitro* and *in vivo* PAI studies of BDT-TBZ CPNs were conducted at University of Macau with a designed PAI system at a wavelength of 1064 nm. For *in vitro* PAI, an aqueous solution of BDT-TBZ CPNs at different concentrations (0, 25, 50, 100, and 200 μg mL$^{-1}$) was placed in the designed PAI system for PA signal collection. For *in vivo* PAI, Balb/c nude mice ($n$ = 3) bearing 4T1 tumor were intravenously injected with BDT-TBZ CPNs at a dose of 2.0 mg kg$^{-1}$, and the PA signal was recorded at various time points after injection of CPNs. During the *in vivo* PAI experiments, mice were anesthetized using the isoflurane anesthesia system all the time. Matlab software was used to analyze the data and generate PA images.

### 2.10 *In vivo* photothermal therapy

When the 4T1 tumor reached approximately 60 mm$^3$ in volume, the Balb/c nude mice bearing 4T1 tumor were distributed randomly into four groups with 5 mice in every group: (1) mice received an intravenous injection of 200 μL PBS solution as a control group; (2) mice received an intravenous injection of 200 μL BDT-TBZ CPNs solution in 1× PBS buffer as CPNs group; (3) mice received irradiation of a 1064 nm laser (1 W cm$^{-2}$) for 6 min at the tumor site as laser group; (4) mice received an intravenous injection of 200 μL BDT-TBZ CPNs

solution in 1× PBS buffer, and at 8 h after the injection, irradiation of a 1064 nm laser (1 W cm$^{-2}$) for 6 min at the tumor site as PTT group. The temperature profiles of mice in the laser group and PTT group were recorded using an infrared camera (SC300, Fluke TiR) during the laser irradiation treatment. During the photothermal therapeutic experiments, mice were anesthetized using the isoflurane anesthesia system all the time. After the therapeutic treatment, the length and width of the 4T1 tumors were recorded with an electronic caliper every two days. Tumor volume was calculated according to the formula: V (volume) = length × width$^2$/2. The bodyweight of mice was also measured during the therapeutic period. $CO_2$ exposure was introduced for the sacrifice of the mice after 14 days of treatment. Selected organ tissues including the heart, liver, spleen, lung, and kidneys were harvested for hematoxylin and eosin (H&E) staining.

### 2.11 *In vivo* biodistribution and hematological analysis

To investigate the *in vivo* biodistribution of BDT-TBZ CPNs, NIR775-doped CPNs were prepared and then intravenously injected into nude mice at a dose of 2.0 mg kg$^{-1}$ ($n = 3$). The mice blood samples were harvested at designated time points (0, 1, 6, 24, 72 h). The major organs (including the brain, heart, lung, liver, spleen, and kidneys) were also collected at 6 and 72 h after the injection. The fluorescence intensity of the blood samples was determined and analyzed. The organs were also imaged using the Lumina XR III *In Vivo* Imaging System (IVIS) to detect the fluorescence intensity. The obtained fluorescence data was analyzed using IVIS Image Analysis Software. To investigate the long-term *in vivo* toxicity, BDT-TBZ CPNs were intravenously injected into nude mice at a dose of 2.0 mg kg$^{-1}$ ($n = 3$). At day 1, 7, and 14, 20 μL blood was harvested from each nude mouse and subsequent hematological analysis was performed using an HLIFE blood analyzer. Mice blood samples collected before the CPNs injection were set as control. The obtained mouse blood routine indexes were shown as mean ± SD deviation.

## 3. Results and discussion

### 3.1 Preparation and characterization of BDT-TBZ CPNs

In this work, through the palladium-catalyzed Stille coupling polymerization, we successfully designed and synthesized the conjugated polymer poly([2,5-bis(2-decyltetradecyl)-2,5-dihydropyrrolo[3,4-*c*]pyrrole-1,4-dione-3,6-dithienyl]-*co*-[6-(2-ethyl-hexyl)-[1,2,5]thiadiazolo [3,4-*f*]benzotriazole-4,8-diyl]) (BDT-TBZ, Fig. 1a) in accordance with the synthetic routes shown in Fig. S1.† Benzodithiophene (BDT) is an excellent electron donor that has been widely adopted for designing novel conjugated molecules and polymers, and thiadiazolobenzotriazole (TBZ) is a strong electron-deficient acceptor.[41,47] With a classic D–A structure, the as-synthesized polymer would possess a planar structure, large extinction coefficient, and narrow energy bandgap, contributing to the strong optical absorption in extended wavelength to NIR-II window. Gel permeation

chromatography (GPC) tests were firstly performed to investigate the physical profile of obtained polymers. As shown in Fig. S2,† the BDT-TBZ polymer has a number-average molecular weight ($M_n$) of 472 Da and a weight-averaged molecular weight (Mw) of 483 Da, with a polymer dispersity index (PDI) of 1.02. The absorption spectra of BDT-TBZ polymer in THF was also determined. The results indicated the strong absorption of BDT-TBZ polymer in the NIR region (Fig. S3†).

The BDT-TBZ CPNs were then prepared *via* a well-established nanoprecipitation approach for *in vitro* and *in vivo* PTT application, and functional polymers polystyrene-polyethylene glycol-carboxyl (PS-PEG-COOH) were co-condensed with BDT-TBZ polymers during the preparation of BDT-TBZ CPNs (Fig. 1). PS-PEG-COOH with hydrophilic side chains not only functions as a hydrotrope to improve the hydrophilia and colloidal stability but also significantly reduces nonspecific adsorption of CPNs for biological studies.[48] As shown in Fig. 2a, dynamic light scattering (DLS) measurements indicated that the hydrodynamic diameter of BDT-TBZ CPNs is about 20 nm with narrow size distribution. The zeta potential of BDT-TBZ CPNs was measured to be −50.4 mV in a translucent aqueous solution, as shown in Fig. S4.† The representative transmission electron microscopy (TEM) image confirmed the monodispersed spherical morphology of BDT-TBZ CPNs, and the observed diameter size of BDT-TBZ CPNs was in good agreement with the DLS results (Fig. 2b). The CPNs aqueous solution remained clear and no significant change in hydrodynamic size was observed upon storage for about a month, indicating the excellent long-term colloidal stability of BDT-TBZ CPNs (Fig. S5†). The optical absorption spectra of BDT-TBZ CPNs in aqueous solution was shown in Fig. 2c. As expected, the BDT-TBZ CPNs exhibited strong absorption in the NIR region with an absorption peak at about 970 nm, extending the absorption wavelength into the NIR-II biological window.

Given that the strong absorption of BDT-TBZ CPNs in the NIR region, we proceeded to investigate the photothermal properties of BDT-TBZ CPNs. High laser power intensity could cause damage to the healthy tissues, induce inflammation, or cause cancer recurrence and metastasis.[49] So it is essential to control the laser power intensity within its maximum permissible exposure (MPE). Considering the distinct MPE for light in different NIR windows, we measured and compared the temperature elevations of BDT-TBZ CPNs under laser irradiation of 808 nm laser (NIR-I window) or 1064 nm laser (NIR-II window) at their respective MPE (0.3 W cm$^{-2}$ for 808 nm and 1 W cm$^{-2}$ for 1064 nm).[27,50] The 980 nm laser was not applied in this study due to the strong water absorption peak at 980 nm, which lead to a rapid increase in tissue temperature.[51] As shown in Fig. 2d, the temperature of BDT-TBZ CPNs aqueous solution (100 μg mL$^{-1}$) under 808 nm laser irradiation at its MPE (0.3 W cm$^{-2}$) was a little bit higher than that irradiated under 1064 nm laser at the same power density. Nevertheless, the temperature achieved by 808 nm laser irradiation at 0.3 W cm$^{-2}$ cannot fulfill the threshold temperature (42 °C) that is required in PTT treatment to induce cancer cell apoptosis and
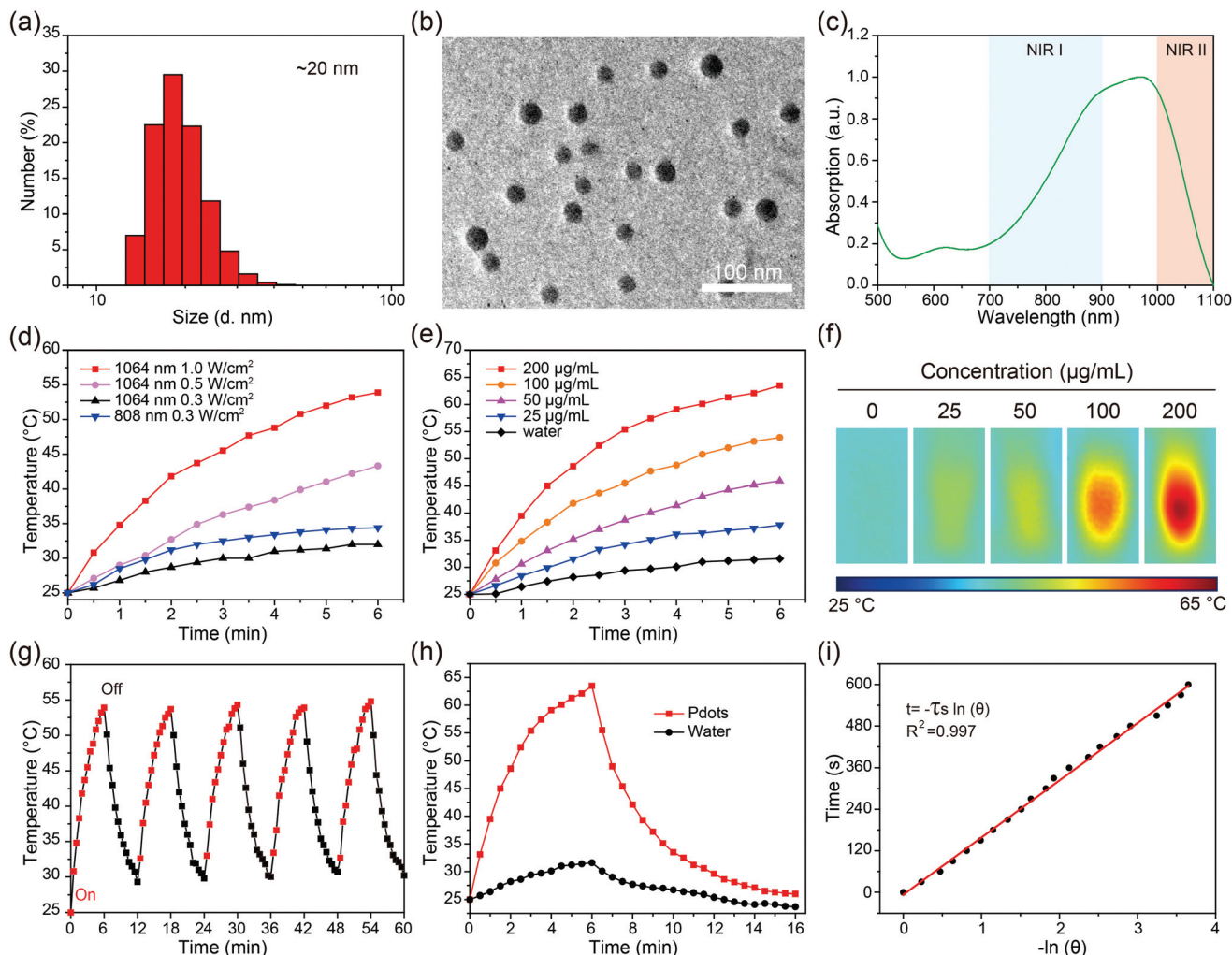
**Fig. 2** Characterization of BDT-TBZ CPNs. (a) Size distribution of BDT-TBZ CPNs measured by DLS. (b) Representative TEM image of BDT-TBZ CPNs. (c) The normalized absorption spectrum of BDT-TBZ CPNs aqueous dispersion. (d) The temperature evolution of BDT-TBZ CPNs aqueous dispersion (100 μg mL$^{-1}$) under irradiation of 1064 nm laser at various power densities (0.3, 0.5, and 1.0 W cm$^{-2}$) or 808 nm laser at relative MPE (0.3 W cm$^{-2}$). (e) The temperature evolution of BDT-TBZ CPNs aqueous dispersions of various concentrations (0, 25, 50, 100, 200 μg mL$^{-1}$) under irradiation of 1064 nm laser at 1.0 W cm$^{-2}$. (f) Corresponding infrared thermal images of BDT-TBZ CPNs aqueous dispersions under irradiation (1 W cm$^{-2}$) for 6 min. (g) Temperature evolution of the BDT-TBZ CPNs solution (100 μg mL$^{-1}$) under irradiation (1 W cm$^{-2}$) for five laser on/off cycles. (h) Photothermal heating and cooling of BDT-TBZ CPNs and water under 1064 nm laser irradiation. (i) Linear time data *versus* −ln θ obtained from the cooling curve in (h).

necrosis.[52] Thus, to achieve temperature higher than threshold temperature, employing a 1064 nm laser would be a better choice due to its higher MPE. We also investigated the temperature elevations of BDT-TBZ CPNs aqueous dispersion solution (100 μg mL$^{-1}$) under 1064 nm laser irradiation (1.0 W cm$^{-2}$) for loner time (10 min). As shown in Fig. S6,† the temperature under 1064 nm laser irradiation can saturate in 10 min. Fig. 2d clearly revealed that increased temperature could be achieved by increasing the power density of 1064 nm laser up to its MPE. When the power density was fixed at its MPE (1 W cm$^{-2}$), the temperature of BDT-TBZ CPNs solution exhibited concentration-dependent elevation, while little change in temperature was observed for water (Fig. 2e). The threshold temperature, 42 °C, could be fulfilled at a relatively

low concentration of 50 μg mL$^{-1}$. A temperature higher than 60 °C was observed under irradiation of 1064 nm laser when the concentration was increased to 200 μg mL$^{-1}$. Fig. 2f displays the corresponding infrared thermal images of BDT-TBZ CPNs dispersions of various concentrations under 1064 nm laser irradiation, again indicating the concentration-dependent photothermal effect of BDT-TBZ CPNs. We then studied the photothermal stability of BDT-TBZ CPNs as it's an essential consideration evaluating the practicality of obtained CPNs for further PTT trials. A cycling laser irradiation process was performed, and the temperature changes of BDT-TBZ CPNs solution under 1064 nm laser irradiation was recorded. As illustrated in Fig. 2g, no significant change in maximum temperature was observed during the five heating/cooling cycles,

clearly manifesting the strong resistibility of BDT-TBZ CPNs upon laser irradiation and temperature variation. Size distribution and absorption spectra profiles of BDT-TBZ CPNs solution before and after laser irradiation were also measured. As shown in Fig. S7 and S8,† negligible change was detected in the above-mentioned properties, further confirming the exceptional photothermal stability of BDT-TBZ CPNs. The photothermal conversion efficiency (PCE) of BDT-TBZ CPNs was also determined as it is a key factor for the evaluation of the capacity in converting light to heat. The PCE of BDT-TBZ CPNs was calculated to be 55% in accordance with the previously reported methods (Fig. 2h and i, the detailed calculation is provided in the ESI†),[45,53] which is comparable to previously reported inorganic and organic NIR-II PTT nanoagents (Table S1, ESI†).[9,27,50,54–58] The strong absorption in the NIR-II biological window, high photothermal conversion efficiency and excellent photothermal stability assure the beneficial utilization of BDT-TBZ CPNs as NIR-II light-responsive PTT nanoplatforms.

## 3.2 *In vitro* PTT of BDT-TBZ CPNs

Previous reports have demonstrated that CPNs could continuously enter cells in an energy-dependent, caveolae-mediated endocytosis pathway despite the negative surface charge,[59,60] encouraging us to continue with the *in vitro* PTT of BDT-TBZ CPNs. To employ the BDT-TBZ CPNs for *in vitro* and *in vivo* PTT trials, we first evaluated the cytotoxicity of BDT-TBZ CPNs *via* the typical 3-(4,5-dimethylthiazol-2-yl)-2,5-diphenyltetrazolium bromide (MTT) assays. As shown in Fig. 3a and S9,† high cell viability of MCF-7 breast cancer cells or 4T1 mammary carcinoma cells was observed (>95%) after incubation with BDT-TBZ CPNs for 24 h or 48 h even when the concentration

reached as high as 100 µg mL$^{-1}$, demonstrating the remarkable biocompatibility of BDT-TBZ CPNs. Nevertheless, significant growth inhibition of cancer cells was observed when BDT-TBZ CPNs-incubated cells were exposed to 1064 nm laser irradiation at a power density of 1 W cm$^{-1}$, as illustrated in Fig. 3b and c. Under laser irradiation, cell viability of MCF-7 and 4T1 cells dramatically declined with the increasing concentration of BDT-TBZ CPNs. Less than 10% of MCF-7 or 4T1 cells were ablated at the concentration of 25 µg mL-1, while over 80% of cancer cells were eradicated after irradiation when the concentration of BDT-TBZ CPNs was increased to 100 µg mL$^{-1}$. Considering that the laser irradiation itself had no suppression effect on cell viability, we can conclude that the decreased cell viability was a result of apoptosis or necrosis induced by the temperature elevation due to the photothermal conversion effect of BDT-TBZ CPNs. Previous reports demonstrated that apoptosis and necrosis are the two fundamental mechanisms of PTT-induced cancer cell death, depending on the laser power density and irradiation time.[61,62] The necrosis triggered by the PTT treatment is considered to be a more passive and immediate form of cell death, which is due to the severe damage of the heat stimuli to the cancer cells.[61] The apoptosis induced by PTT treatment is shown to be mediated by the intrinsic mitochondrial pathway through the activation of the Bid protein.[62] To further visualize the PTT efficacy of BDT-TBZ CPNs, we performed the living/dead cell staining assay. MCF-7 cells received various treatments were co-stained with calcein-AM and PI so that living (green) and dead (red) cells can be distinguished under fluorescence microscopy. Strong green fluorescence can be observed for the cells incubated with BDT-TBZ CPNs or irradiated under 1064 nm laser, while cells were then stained by red fluorescence when treated with BDT-TBZ CPNs incubation and subsequent laser irradiation (Fig. 3d). The confocal fluorescence imaging result was consistent with the MTT assays, confirming the remarkable *in vitro* PTT efficacy of BDT-TBZ CPNs under 1064 nm laser irradiation.

## 3.3 PAI performance of BDT-TBZ CPNs

Motivated by the efficient photothermal performance of BDT-TBZ CPNs, we investigated the feasibility of the CPNs as PAI contrast agents with a lab-built PAI system (Fig. S10†). The photoacoustic imaging performance of BDT-TBZ CPNs in aqueous solution was evaluated and the PA images of CPNs at various concentrations were shown in Fig. 4a. The background signal, laser intensity variation, and the sensitivity of the transducers of the PA imaging system result in the inhomogeneous signal intensity in the reconstructed image. Similar findings were also demonstrated in previous publications.[9,50,57] The obtained data were quantified and analyzed as Fig. 4b, clearly indicating the excellent PA performance of the CPNs as PA signal intensity dramatically increased with increasing concentrations of CPNs. It is worth pointing out that the PA signal intensity of as-obtained CPNs exhibited an obvious linear correlation with the concentration, which is essential for future quantitative analysis of PAI. Thereafter, the *in vivo* PAI capa-
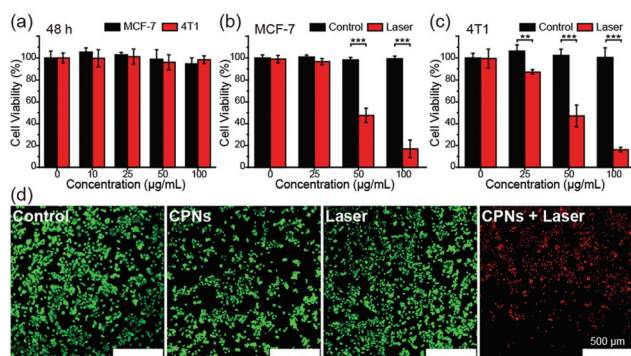


Fig. 3 *In vitro* PTT of BDT–TBZ CPNs. (a) MTT assays to access the relative cell viability of MCF-7 and 4T1 cells after incubation with different concentrations of BDT-TBZ CPNs for 48 h. Error bars indicate standard deviation (n = 6). MTT assays to access the relative cell viability of (b) MCF-7 cells or (c) 4T1 cells treated with BDT-TBZ CPNs incubation for 12 h at various concentrations with or without subsequent 1064 nm laser irradiation (1 W cm$^{-1}$, 6 min). Error bars indicate standard deviation (n = 6). (t test unpaired analysis, ** $p$ < 0.01, *** $p$ < 0.001) (d) Representative confocal fluorescence images of MCF-7 cells co-stained with by calcein-AM (living cells, green) and PI (dead cells, red) after various treatments. Scale bar: 500 µm.
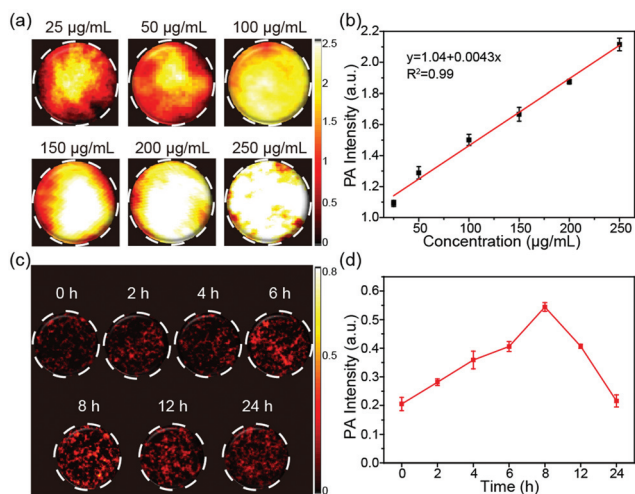
Fig. 4 PAI performance of BDT-TBZ CPNs. (a) The PA images of BDT-TBZ CPNs solutions at various concentrations (25, 50, 100, 150, 200, and 250 μg mL$^{-1}$). (b) The PA signal intensity of BDT-TBZ CPNs at various concentrations and the corresponding linear correlation between PA intensity and concentrations ($n$ = 3). (c) *In vivo* PA images of the tumor site at various time intervals (0, 2, 4, 6, 8, 12, and 24 h) after intravenous injection of BDT-TBZ CPNs (at a dose of 2.0 mg kg$^{-1}$) into nude mice. (d) The PA signal intensity variation at the tumor site after intravenous injection of BDT-TBZ CPNs into nude mice. Error bars indicate standard deviation ($n$ = 3).

bility of BDT-TBZ CPNs was examined in 4T1 tumor-bearing nude mice. After intravenous administration of BDT-TBZ CPNs solution in 1× PBS buffer in the mice, the tumor site was monitored, and the PA signals were collected under 1064 nm laser irradiation at designated time points. The generated PA images and relevant quantified data were shown in Fig. 4c and d. After administering the BDT-TBZ CPNs, the PAI signal intensity at the tumor site gradually enhanced *versus* time. The PAI contrast enhancement indicated the efficient accumulation of the CPNs in the tumor mainly attributed to the enhanced permeability and retention (EPR) effect.[63] At 8 h post-injection, the PA signal intensity at the tumor site reached to the maximum and started to gradually decline to lower intensity, revealing that the optimal time for cancer PTT is 8 h after the injection of the CPNs. We compared the PA result with our previously developed PA agents that were imaged with the same PA imaging system as in this work to make sure the comparison is under the same standard. As shown in Table S2 (ESI†), the BDT-TBZ CPNs used in this work exhibited the highest PA signal intensity enhancement even compared to the other PA nanoagents that were intratumorally injected, indicating the superiority of the BDT-TBZ CPNs as a PA imaging agent.[45,64,65] The PTT efficacy could be significantly improved under the guideline of PAI results *via* the determination of the optimal time for cancer treatment, further confirming the necessity and significance of the development of theranostic nanoplatforms for PAI-guided cancer PTT.

## 3.4  *In vivo* PTT of BDT-TBZ CPNs

Encouraged by the outstanding PTT and PAI performance, we continued to study the *in vivo* PTT therapeutic efficacy of BDT-TBZ CPNs on the 4T1 tumor xenograft model. When the tumor size reached approximately 80 mm$^3$, the mice were distributed in four random groups ($n$ = 5). In the PTT group, the mice received an intravenous injection of CPNs and followed by irradiation of 1064 nm laser at a power density of 1 W cm$^{-1}$ for 6 min. The laser irradiation at the tumor site was performed at 8 h after CPNs injection according to the *in vivo* PAI results. The other three groups included untreated mice (Control group), CPNs-injected mice (CPNs group), and laser-irradiated mice injected with PBS (Laser group). Temperature change at the tumor site of the mice was monitored during the 1064 nm laser irradiation in both the Laser and PTT groups (Fig. 5a). Accordingly, quantitative data in Fig. 5b indicated that the temperature at the tumor site (56 °C) after irradiation in the PTT group was significantly higher than that (40 °C) in the Laser group. The rapid temperature elevation certifies the sufficient accumulation of the CPNs in the tumor during the blood circulation and the efficient *in vivo* photothermal conversion. The tumor volume was monitored and recorded every two days after different treatments. As shown in Fig. 5c and S11,† the tumors in the PTT group were significantly suppressed after the treatment and no recurrence was observed in 14 days, while the tumors in the other three groups showed a similarly rapid growth tendency during the treatment period. The harvested tumors and the corresponding tumor weight data were shown in Fig. 5d and S12,† showing that the solid tumors in 3 out of 5 mice were completely ablated in the PTT group which proves the remarkable antitumor efficiency of the PTT treatment. We added the laser power density for *in vivo* experiments of the PTT agents listed in Table S1 (ESI†) for comparison. As shown, the irradiation condition in this work is milder than that of the majority listed PTT agents in Table S1 (ESI†). In addition, the body weight data of mice from these groups showed no obvious differences among the various treatments throughout the entire therapeutic period, revealing the insignificant systemic side effects of the CPNs-medicated PTT cancer treatment (Fig. 5e). More importantly, histological and histomorphometric analyses were also conducted with collected organs after the treatment. As shown in Fig. 5f, no appreciable histopathological abnormality in H&E staining assays was observed in organs harvested from mice of the PTT group and the Control group, demonstrating the favorable biocompatibility of the BDT-TBZ CPNs for normal tissues in the case of no irradiation. The histological and histomorphometric assays demonstrated the superior biocompatibility of the BDT-TBZ CPNs in the PTT cancer therapy. It should be noticed that a relatively high temperature is required in the PTT to achieve cancer cell death and tumor elimination, driving scientists devoted to developing the nanoplatforms that have the highest possible absorption, extinction coefficients, and photothermal conversion efficiency for a better PTT effect.[66] In addition, many strategies could be used to
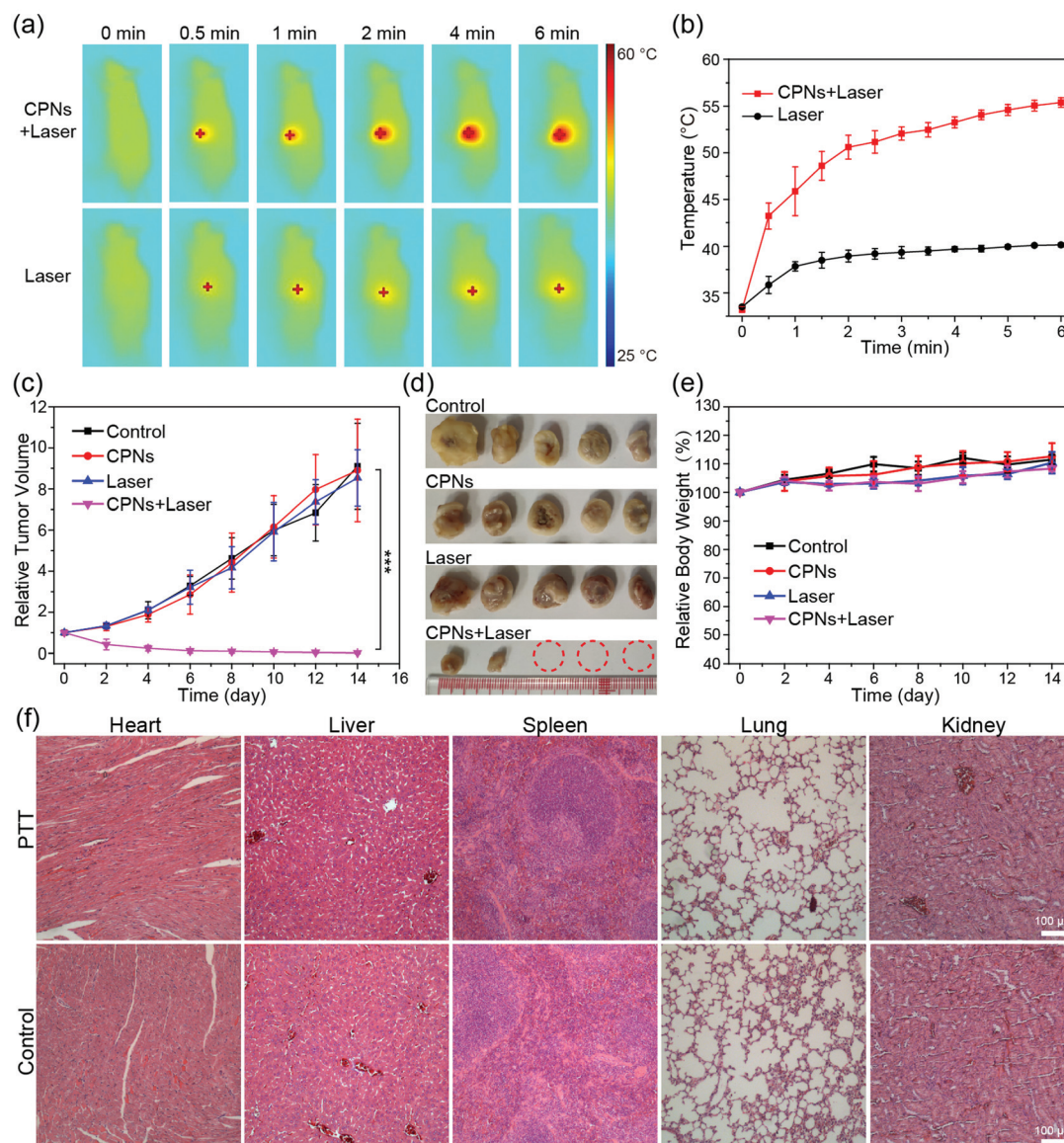
**Fig. 5** *In vivo* PTT of BDT–TBZ CPNs. (a) Photothermal infrared thermal images of mice bearing 4T1 tumor under the 1064 nm NIR-II laser irradiation (1 W cm$^{-2}$) with intravenous injection of BDT–TBZ CPNs (200 μg mL$^{-1}$) or PBS (at a dose of 2.0 mg kg$^{-1}$). (b) Temperature changes at the tumor site during the laser irradiation for the PTT and Control group in (a). (c) Relative tumor volume of mice after various treatments (*t* test unpaired analysis, *** $p < 0.001$). (d) Photographs of tumors harvested at 14th day after various treatments. (e) Relative body weight of mice after various treatments. (f) Histology H&E staining of organ tissues harvested from the PTT and Control groups of mice at 14th day after various treatments. Scale bar: 100 μm. Error bars indicate standard deviation (*n* = 5).

reduce the side effects, such as, modification of CPNs with active cancer cell-targeting ability to enhance the accumulation of CPNs in the tumor, or combining PTT with other therapeutic modalities for enhanced therapeutic effect. In spite of the potential challenge, NIR-II responsive PTT is still considered to be a compelling therapeutic modality holding great clinical translational potential.[2,30]

### 3.5 *In vivo* metabolism and toxicity

The concern upon the long-term *in vivo* metabolism and toxicity of nanomedicines is still the dominant limitation for

their potential clinical utilizations. Thus, we conducted *in vivo* tests to determine the above-mentioned properties of the BDT–TBZ CPNs. To understand the metabolism pathway, silicon 2,3-naphthalocyanine bis(trihexylsilyloxide) (NIR775)-doped CPNs were prepared so that the *in vivo* dynamic biodistribution and clearance of CPNs could be imaged and tracked *via* fluorescence imaging with the *In Vivo* Imaging System (IVIS). The DLS profile suggested that the size of the CPNs were negligibly influenced by NIR 775 doping (Fig. S13†). Then, we investigated the fluorescence stability of NIR 775-doped CPNs solutions at different time intervals (0, 1, 2,

and 3 d). As shown in Fig. S14,† the fluorescence intensity of NIR 775-doped CPNs exhibited negligible changes in 3 days, indicating the good stability of NIR 775-doped CPNs. After intravenous injection of NIR 775-doped CPNs into Balb/c nude mice, the blood samples at designated time points (0, 1, 6, 24, 72 h) were harvested and analyzed. As illuminated in Fig. 6a, intense fluorescence signal was detected in the blood at 1 h post-injection, and the fluorescence intensity declined fast along the time. The major organs were also collected after the intravenous injection and imaged. As shown in Fig. 6b, strong fluorescence signal was detected in the liver at 6 h post-injection, whereas almost no fluorescence was observed from other organs. The liver accumulation might be due to the uptake and enrichment of the CPNs in the reticuloendothelial system during the blood circulation, suggesting the potential clearance of CPNs through the biliary pathway.[10,50,67] Also, no fluorescence could be detected at 72 h after injection, indicating the quick removal of the CPNs from the body. Together, these data demonstrates the rapid body clearance of the BDT-TBZ CPNs, confirming the excellent metabolizability of the obtained CPNs. Additionally, the long-term toxicology of the BDT-TBZ CPNs was accessed by performing the hematological analyses. After the intravenous injection of the CPNs, the blood samples of nude mice were collected at designated time points (0, 1, 7, 14 d) and analyzed. Blood samples at day 0 refer to the collected blood before the injection of CPNs. According to the data shown in Fig. 6c, the blood routine indexes of the CPNs-injected mice displayed no significant

difference compared to the control samples, demonstrating the insignificant hepatotoxic effects of the CPNs. Biocompatibility is an essential consideration for nanoparticles aimed at biological and biomedical applications. As a class of nanomaterials completely composed of organic and biologically inert components, conjugated polymer nanoparticles (CPNs) possess good biocompatibility by intrinsically avoiding the potential toxicity of heavy metal ions.[68] Rao and coworkers conducted a pre-clinically systematic toxicity evaluation, demonstrating that the intravenous injection of CPNs did not lead to unusual behavior as well as acute or chronic toxicity in balb/c mice.[69] Ding *et al.* evaluated the toxicity of CPNs in ICR mice and observed no obvious abnormality to the functions of liver and kidney organs of mice.[70] Taken together with our *in vivo* metabolism and toxicity data, we can confirm the favorable biological compatibility of the BDT-TBZ CPNs in cancer theranostics.

# 4. Conclusions

In summary, we successfully synthesized the metabolizable theranostic nanoagents of conjugated BDT-TBZ CPNs with strong absorption in the NIR-II region, high photothermal conversion efficiency, excellent thermal stability, and negligible cytotoxicity. BDT-TBZ CPNs could also be employed as attractive PAI contrast agents due to the remarkable PA signal generation capability both *in vitro* and *in vivo*. Based on the PAI guideline, BDT-TBZ CPNs achieved excellent photothermal therapeutic performance under 1064 nm laser irradiation with efficient cancer cell ablation and significant tumor suppression. Notably, BDT-TBZ CPNs exhibited rapid body clearance property and demonstrated no systematic toxicity and side effects, indicating superior biocompatibility. Therefore, BDT-TBZ CPNs hold great potential for precise and efficient near-infrared II PAI guided PTT and provide new insights into the clinical translation of theranostic nanoplatforms for anticancer therapy.



**Fig. 6** *In vivo* metabolism and toxicity of BDT-TBZ CPNs. (a) Relative fluorescence intensity of BDT-TBZ CPNs in mice blood at designated time points after the intravenous injection (at a dose of 2.0 mg kg$^{-1}$). (b) Fluorescence imaging of organs harvested at designated time points after the intravenous injection of BDT-TBZ CPNs. (c) The blood routine indexes at designated time points of mice received intravenous injection BDT-TBZ CPNs. (WBC: white blood cell, RBC: red blood cell, HGB: hemoglobin, and PLT: platelet; LYM: lymphocyte; MON: mononuclear cell). Error bars indicate standard deviation (*n* = 3).

# Author contributions

F. W., and X. M. contributed equally to this work. F. W., X. M., Z. Y. and P. K. L. conceived the study; F. W. and X. M. performed the *in vitro* and *in vivo* PTT experiments; H. C. synthesized and provided BDT-TBZ; X. M. and M. X. performed PAI experiments. F. W., F. M., and X. X. M. performed *in vivo* toxicity experiments. All of the authors reviewed and contributed to the manuscript.

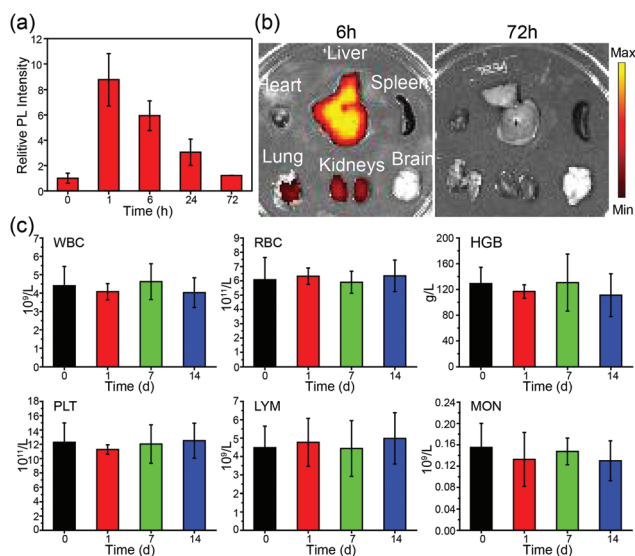# Conflicts of interest

There are no conflicts to declare.

## Acknowledgements

## Notes and references

1 R. L. Siegel, K. D. Miller and A. Jemal, *Ca-Cancer J. Clin.*, 2019, **69**, 7–34.

2 L. Cheng, C. Wang, L. Z. Feng, K. Yang and Z. Liu, *Chem. Rev.*, 2014, **114**, 10869–10939.

3 D. Jaque, L. M. Maestro, B. del Rosal, P. Haro-Gonzalez, A. Benayas, J. L. Plaza, E. M. Rodriguez and J. G. Sole, *Nanoscale*, 2014, **6**, 9494–9530.

4 M. G. van der Vaart, R. Meerwaidt, R. H. J. A. Slart, G. M. van Dam, R. A. Tio and C. J. Zeebregts, *Eur. J. Vasc. Endovasc. Surg.*, 2008, **35**, 507–513.

5 J. W. Kim, E. I. Galanzha, E. V. Shashkov, H. M. Moon and V. P. Zharov, *Nat. Nanotechnol.*, 2009, **4**, 688–694.

6 J. Wallyn, N. Anton, S. Akram and T. F. Vandamme, *Pharm. Res.*, 2019, **36**, 78.

7 K. Y. Pu, A. J. Shuhendler, J. V. Jokerst, J. G. Mei, S. S. Gambhir, Z. N. Bao and J. H. Rao, *Nat. Nanotechnol.*, 2014, **9**, 233–239.

8 Y. J. Liu, P. Bhattarai, Z. F. Dai and X. Y. Chen, *Chem. Soc. Rev.*, 2019, **48**, 2053–2108.

9 Y. Gao, F. Wang, W. Huang, C. Yang, W. Guo, C. Song, Q. Zhang, B. Yang, Y. Xu and C. Guo, *Nanoscale*, 2019, **11**, 3300–3310.

10 S. J. Liu, X. Zhou, H. K. Zhang, H. L. Ou, J. W. Y. Lam, Y. Liu, L. Q. Shi, D. Ding and B. Z. Tang, *J. Am. Chem. Soc.*, 2019, **141**, 5359–5368.

11 V. Shanmugam, S. Selvakumar and C. S. Yeh, *Chem. Soc. Rev.*, 2014, **43**, 6254–6287.

12 K. Yang, S. A. Zhang, G. X. Zhang, X. M. Sun, S. T. Lee and Z. A. Liu, *Nano Lett.*, 2010, **10**, 3318–3323.

13 X. W. Liu, H. Q. Tao, K. Yang, S. A. Zhang, S. T. Lee and Z. A. Liu, *Biomaterials*, 2011, **32**, 144–151.

14 D. Ding, W. Guo, C. Guo, J. Sun, N. Zheng, F. Wang, M. Yan and S. Liu, *Nanoscale*, 2017, **9**, 2020–2029.

15 G. X. Lv, W. S. Guo, W. Zhang, T. B. Zhang, S. Y. Li, S. Z. Chen, A. S. Eltahan, D. L. Wang, Y. Q. Wang, J. C. Zhang, P. C. Wang, J. Chang and X. J. Liang, *ACS Nano*, 2016, **10**, 9637–9645.

16 H. H. Xie, M. Q. Liu, B. H. You, G. H. Luo, Y. Chen, B. L. Liu, Z. Y. Jiang, P. K. Chu, J. D. Shao and X. F. Yu, *Small*, 2020, **16**, 1905208.

17 W. Guo, F. Wang, D. D. Ding, C. Q. Song, C. S. Guo and S. Q. Liu, *Chem. Mater.*, 2017, **29**, 9262–9274.

18 T. Liu, Y. Chao, M. Gao, C. Liang, Q. Chen, G. S. Song, L. Cheng and Z. Liu, *Nano Res.*, 2016, **9**, 3003–3017.

19 F. Wang, C. Song, W. Guo, D. Ding, Q. Zhang, Y. Gao, M. Yan, C. Guo and S. Liu, *New J. Chem.*, 2017, **41**, 14179–14187.

20 C. Y. Zhou, L. Zhang, T. Sun, Y. Zhang, Y. D. Liu, M. F. Gong, Z. S. Xu, M. M. Du, Y. Liu, G. Liu and D. Zhang, *Adv. Mater.*, 2021, **33**, 2006532.

21 S. B. Zhang, W. S. Guo, J. Wei, C. Li, X. J. Liang and M. Z. Yin, *ACS Nano*, 2017, **11**, 3797–3805.

22 Q. Wang, B. Xia, J. Z. Xu, X. R. Niu, J. Cai, Q. M. Shen, W. J. Wang, W. Huang and Q. L. Fan, *Mater. Chem. Front.*, 2019, **3**, 650–655.

23 X.-Q. Xu, H. Liao, H. Liu, Y. Chu, Y. He and Y. Wang, *CCS Chem.*, 2020, 2520–2529.

24 N. Alifu, A. Zebibula, J. Qi, H. Q. Zhang, C. W. Sun, X. M. Yu, D. W. Xue, J. W. Y. Lam, G. H. Li, J. Qian and B. Z. Tang, *ACS Nano*, 2018, **12**, 11282–11293.

25 H. Zhou, X. D. Zeng, A. G. Li, W. Y. Zhou, L. Tang, W. B. Hu, Q. L. Fan, X. L. Meng, H. Deng, L. Duan, Y. Q. Li, Z. X. Deng, X. C. Hong and Y. L. Xiao, *Nat. Commun.*, 2020, **11**, 6183.

26 A. M. Smith, M. C. Mancini and S. M. Nie, *Nat. Nanotechnol.*, 2009, **4**, 710–711.

27 Y. Y. Jiang, J. C. Li, X. Zhen, C. Xie and K. Y. Pu, *Adv. Mater.*, 2018, **30**, 1705980.

28 C. F. Wu and D. T. Chiu, *Angew. Chem., Int. Ed.*, 2013, **52**, 3086–3109.

29 J. B. Yu, Y. Rong, C. T. Kuo, X. H. Zhou and D. T. Chiu, *Anal. Chem.*, 2017, **89**, 42–56.

30 C. Yin, X. Lu, Q. Fan and W. Huang, *View*, 2021, **2**, 20200070.

31 Z. Liu, J. Liu, Z. Sun, Z. Zhang, Y. Yuan, X. Fang, F. Wang, W. Qin and C. Wu, *Anal. Chem.*, 2019, **91**, 4179–4185.

32 X. Q. Shen, L. Li, H. Wu, S. Q. Yao and Q. H. Xu, *Nanoscale*, 2011, **3**, 5140–5146.

33 Q. Q. Miao, C. Xie, X. Zhen, Y. Lyu, H. W. Duan, X. G. Liu, J. V. Jokerst and K. Y. Pu, *Nat. Biotechnol.*, 2017, **35**, 1102–1110.

34 Z. Zhang, X. F. Fang, Z. H. Liu, H. C. Liu, D. D. Chen, S. Q. He, J. Zheng, B. Yang, W. P. Qin, X. J. Zhang and C. F. Wu, *Angew. Chem., Int. Ed.*, 2020, **59**, 3691–3698.

35 G. X. Feng, D. Ding, K. Li, J. Liu and B. Liu, *Nanoscale*, 2014, **6**, 4141–4147.

36 J. Y. Sun, H. Mel, S. F. Wang and F. Gao, *Anal. Chem.*, 2016, **88**, 7372–7377.

37 X. Fang, B. Ju, Z. Liu, F. Wang, G. Xi, Z. Sun, H. Chen, C. Sui, M. Wang and C. Wu, *ChemBioChem*, 2019, **20**, 521–525.

38 H. B. Chen, X. F. Fang, Y. Jin, X. Hu, M. Yin, X. J. Men, N. Chen, C. H. Fan, D. T. Chiu, Y. Z. Wan and C. F. Wu, *Small*, 2018, **14**, 1800239.

39 F. Wang, H. Chen, Z. Liu, F. Mi, X. Fang, J. Liu, M. Wang, P. K. Lo and Q. Li, *New J. Chem.*, 2019, **43**, 14443–14449.

40 Y. Lyu, S. S. He, J. C. Li, Y. Y. Jiang, H. Sun, Y. S. Miao and K. Y. Pu, *Angew. Chem., Int. Ed.*, 2019, **58**, 18197–18201.

41 B. Guo, Z. Feng, D. H. Hu, S. D. Xu, E. Middha, Y. T. Pan, C. B. Liu, H. R. Zheng, J. Qian, Z. H. Sheng and B. Liu, *Adv. Mater.*, 2019, **31**, 1902504.

42 C. Yin, G. H. Wen, C. Liu, B. G. Yang, S. E. Lin, J. W. Huang, P. C. Zhao, S. H. D. Wong, K. Y. Zhang, X. Y. Chen, G. Li, X. H. Jiang, J. P. Huang, K. Y. Pu, L. D. Wang and L. M. Bian, *ACS Nano*, 2018, **12**, 12201–12211.

43 B. Zhang, F. Wang, H. Zhou, D. Gao, Z. Yuan, C. Wu and X. Zhang, *Angew. Chem.*, 2019, **58**, 2744–2748.

44 H. J. Zhu, J. C. Li, X. Y. Qi, P. Chen and K. Y. Pu, *Nano Lett.*, 2018, **18**, 586–594.

45 H. B. Chen, J. Zhang, K. W. Chang, X. J. Men, X. F. Fang, L. B. Zhou, D. L. Li, D. Y. Gao, S. Y. Yin, X. J. Zhang, Z. Yuan and C. F. Wu, *Biomaterials*, 2017, **144**, 42–52.

46 C. F. Wu, C. Szymanski and J. McNeill, *Langmuir*, 2006, **22**, 2956–2960.

47 D. Y. Gao, D. H. Hu, X. Liu, X. J. Zhang, Z. Yuan, Z. H. Sheng and H. R. Zheng, *ACS Appl. Polym. Mater.*, 2020, **2**, 4241–4257.

48 J. Y. Sun, Q. Zhang, X. M. Dai, P. H. Ling and F. Gao, *Chem. Commun.*, 2021, **57**, 1989–2004.

49 M. R. K. Ali, Y. Wu and M. A. El-Sayed, *J. Phys. Chem. C*, 2019, **123**, 15375–15393.

50 X. Men, F. Wang, H. B. Chen, Y. B. Liu, X. X. Men, Y. Yuan, Z. Zhang, D. Y. Gao, C. F. Wu and Z. Yuan, *Adv. Funct. Mater.*, 2020, **30**, 1909673.

51 L. F. Lu, B. H. Li, S. W. Ding, Y. Fan, S. F. Wang, C. X. Sun, M. Y. Zhao, C. X. Zhao and F. Zhang, *Nat. Commun.*, 2020, **11**, 4192.

52 W. T. Sun, K. Ge, Y. Jin, Y. Han, H. S. Zhang, G. Q. Zhou, X. J. Yang, D. D. Liu, H. F. Liu, X. J. Liang and J. C. Zhang, *ACS Nano*, 2019, **13**, 7556–7567.

53 D. K. Roper, W. Ahn and M. Hoepfner, *J. Phys. Chem. C*, 2007, **111**, 3636–3641.

54 C. Yin, X. Z. Li, G. H. Wen, B. G. Yang, Y. C. Zhang, X. Y. Chen, P. C. Zhao, S. L. Li, R. Li, L. D. Wang, C. S. Lee and L. M. Bian, *Biomaterials*, 2020, **232**, 119684.

55 Y. Y. Cao, J. H. Dou, N. J. Zhao, S. M. Zhang, Y. Q. Zheng, J. P. Zhang, J. Y. Wang, J. Pei and Y. P. Wang, *Chem. Mater.*, 2017, **29**, 718–725.

56 Z. Zhou, B. W. Li, C. Shen, D. Wu, H. C. Fan, J. Q. Zhao, H. Li, Z. Y. Zeng, Z. M. Luo, L. F. Ma and C. L. Tan, *Small*, 2020, **16**, 2004173.

57 K. M. Ke, W. Yang, X. L. Xie, R. Liu, L. L. Wang, W. W. Lin, G. M. Huang, C. H. Lu and H. H. Yang, *Theranostics*, 2017, **7**, 4763–4776.

58 H. J. Xiang, H. Lin, L. D. Yu and Y. Chen, *ACS Nano*, 2019, **13**, 2223–2235.

59 Y. P. Han, X. M. Li, H. B. Chen, X. J. Hu, Y. Luo, T. Wang, Z. J. Wang, Q. Li, C. H. Fan, J. Y. Shi, L. H. Wang, Y. Zhao, C. F. Wu and N. Chen, *ACS Appl. Mater. Interfaces*, 2017, **9**, 21200–21208.

60 J. H. Lee, M. Twomey, C. Machado, G. Gomez, M. Doshi, A. J. Gesquiere and J. H. Moon, *Macromol. Biosci.*, 2013, **13**, 913–920.

61 X. H. Huang, B. Kang, W. Qian, M. A. Mackey, P. C. Chen, A. K. Oyelere, I. H. El-Sayed and M. A. El-Sayed, *J. Biomed. Opt.*, 2010, **15**, 058002.

62 M. Perez-Hernandez, P. del Pino, S. G. Mitchell, M. Moros, G. Stepien, B. Pelaz, W. J. Parak, E. M. Galvez, J. Pardo and J. M. de la Fuente, *ACS Nano*, 2015, **9**, 52–61.

63 O. C. Farokhzad and R. Langer, *ACS Nano*, 2009, **3**, 16–20.

64 K. W. Chang, Y. B. Liu, D. H. Hu, Q. F. Qi, D. Y. Gao, Y. T. Wang, D. L. Li, X. J. Zhang, H. R. Zheng, Z. H. Sheng and Z. Yuan, *ACS Appl. Mater. Interfaces*, 2018, **10**, 7012–7021.

65 X. J. Men, H. B. Chen, C. Sun, Y. B. Liu, R. B. Wang, X. J. Zhang, C. F. Wu and Z. Yuan, *ACS Appl. Mater. Interfaces*, 2020, **12**, 51174–51184.

66 C. Xu and K. Y. Pu, *Chem. Soc. Rev.*, 2021, **50**, 1111–1137.

67 G. X. Feng, J. Liu, R. R. Liu, D. Mao, N. Tomczak and B. Liu, *Adv. Sci.*, 2017, **4**, 1600407.

68 K. Y. Pu, N. Chattopadhyay and J. H. Rao, *J. Controlled Release*, 2016, **240**, 312–322.

69 A. J. Shuhendler, K. Y. Pu, L. Cui, J. P. Uetrecht and J. H. Rao, *Nat. Biotechnol.*, 2014, **32**, 373–380.

70 D. Ding, J. Liu, G. X. Feng, K. Li, Y. Hu and B. Liu, *Small*, 2013, **9**, 3093–3102.